Environmental Adaptability of Legged Robots with Cutaneous Inflation and Sensation

Taekyoung Kim, Sudong Lee, Shinwon Chang, Saehui Hwang, and Yong-Lae Park*

In this article, a novel approach to enhance the maneuverability and adaptability of legged robots in challenging environments is proposed. This approach involves the integration of soft inflatable sensing skin, which provides additional mobile modes and environmental adaptability. The inflated skin's structural properties, such as buoyancy, volumed shape, and physical compliance, enable quadruped robots to extend their mobility to stable swimming and crawling modes. The inflated skin also offers physical protection through cushioning and backing effects, allowing robots to roll down stair-like structures. Furthermore, the integration of tactile sensors provides the host robot with accurate and intuitive contact information, enabling increased environmental adaptability and responsive behavior. The robot can protect itself from impacts, detect and detour obstacles, and dynamically interact with its surrounding environment. Overall, the proposed approach offers a synergistic integration of soft inflatable sensing skin and tactile sensors to enhance legged robots' maneuverability and adaptability in harsh environments. The integrated system enables robots to achieve challenging missions, extending their capabilities beyond conventional locomotive modes. The proposed approach has significant potential applications in fields such as search and rescue, surveillance, and exploration.

1. Introduction

Mobile robots promise a safer and more efficient future for humankind by performing demanding tasks in harsh conditions, such as search and rescue in disaster sites, exploring rough environments, and performing labor in industrial and agricultural sites.[1–7] To achieve such challenging missions, it is critical that mobile robots are able to operate with high maneuverability and adaptability in dynamic and risky environments. In recent years, legged robots, compared to wheeled or tracked robots, have gained significant attention for their environmentally adaptive maneuverability in various terrains.[8–20] In particular, quadruped robots have achieved impressive advancements in dynamic locomotion modes (e.g., walking, running, jumping) using sophisticated control strategies.[21–24] For instance, ETH's ANYmal and Boston Dynamics' Spot Mini have shown stable walking and running performances in diverse real-world environments, such as uneven terrains, slippery surfaces, and complex human-made facilities.[25–30] MIT's Cheetah 2 was able to jump over obstacles during high-speed running under indoor and outdoor ground conditions.[31,32] More recently, Cheetah 3 showcased jumping in a static state and walking on irregular terrain based on an expanded range of motion.[33–35] Such impressive feats from ANYmal and Cheetah have been possible through optimization-based control strategies, such as model predictive control (MPC), allowing for advanced locomotion while maintaining a stable state.[36] The ETH team additionally applied deep reinforcement learning to ANYmal to allow adaptive walking on various terrains.[37–39]

Additionally, response skills have been applied to quadruped robots, enabling them to adapt to environments by adding suitable hardware components or control strategies. For example, the use of series elastic actuators enabled ANYmal to be more

T. Kim
Department of Materials Science and Engineering
Northwestern University
Evanston, IL 60208, USA

T. Kim, S. Lee
Soft Robotics Research Center
Seoul National University
Seoul 08826, Korea

[iD] The ORCID identification number(s) for the author(s) of this article can be found under https://doi.org/10.1002/aisy.202300172.

S. Lee
CREATE Lab
Institute of Mechanical Engineering, EPFL
1015 Lausanne, Switzerland

S. Chang, Y.-L. Park
Department of Mechanical Engineering
Institute of Advanced Machines and Design
Institute of Engineering Research
Seoul National University
Seoul 08826, Korea
E-mail: ylpark@snu.ac.kr

S. Hwang
Department of Mechanical Engineering
Stanford University
Stanford, CA 94305, USA

tolerant of external disturbances through increased mechanical compliance.[26,40,41] The change in foot type (e.g., wheel and soft feet) improved the applicability of ANYmal under various ground conditions.[24,42,43] Additional manipulators integrated with ANYmal and Spot Mini enabled them to interact with environments, such as opening doors or moving obstacles.[44,45] Moreover, ANYmal's and Spot Mini's robotic arms contribute to maintaining robot balance and recovery after falling.[44] ANYmal is also able to recover from impacts and falling situations by employing machine learning techniques.[46,47]

To ensure high maneuverability of quadruped robots in even harsher landforms, such as terrains with water, confined spaces, and steep slopes, as many additional mobile modes as possible are required to overcome the encountered challenging circumstances.[48] Furthermore, robots should have enhanced capabilities, such as self-defense, autonomy, and dynamic interaction, since robot stability is not always guaranteed in unexpected real-world situations (e.g., falling, unexpected collisions, and low- or no-light conditions).

In this article, we propose a synergistic approach using two recently advanced technologies, which are inflatable sensing skin and legged robots, to enhance the mobility and the environmental adaptive responses of legged robots. In addition, we demonstrate the improved performances of legged robots equipped with the inflatable sensing skin in various realistic situations (**Figure 1** and **2**a). When the skin is inflated, it provides structural properties (Figure 2b), such as buoyancy and mechanical compliance using its volumed form as well as protective effects from physical risk factors. This extends the robot's mobility without adding complex control strategies. In addition, the embedded tactile sensors provide information on the locations and magnitudes of the contact forces (Figure 2c,d), which help the robot adapt to environments by immediately detecting unpredictable disturbances and physical interactions without requiring significant computational costs.

There has been research on inflatable structures for human- and environment-friendly robots.[49–51] For example, Qi et al. developed an entire robotic arm composed of only inflatable chambers.[52] Ohta et al. proposed inflatable sleeves made of heat-sealable polymer sheets designed to cover a robotic arm using pneumatic artificial muscles.[53] However, these inflatable structures did not have sensing functionalities to collect tactile information directly. Kim et al. developed a soft inflatable sensing module made of stretchable silicone elastomer with embedded microfluidic tactile sensing integrated into a robotic arm to detect contact locations and measure the magnitude of applied external contacts.[54] However, the high-density materials made the structure heavy, and casting silicone into various shapes for
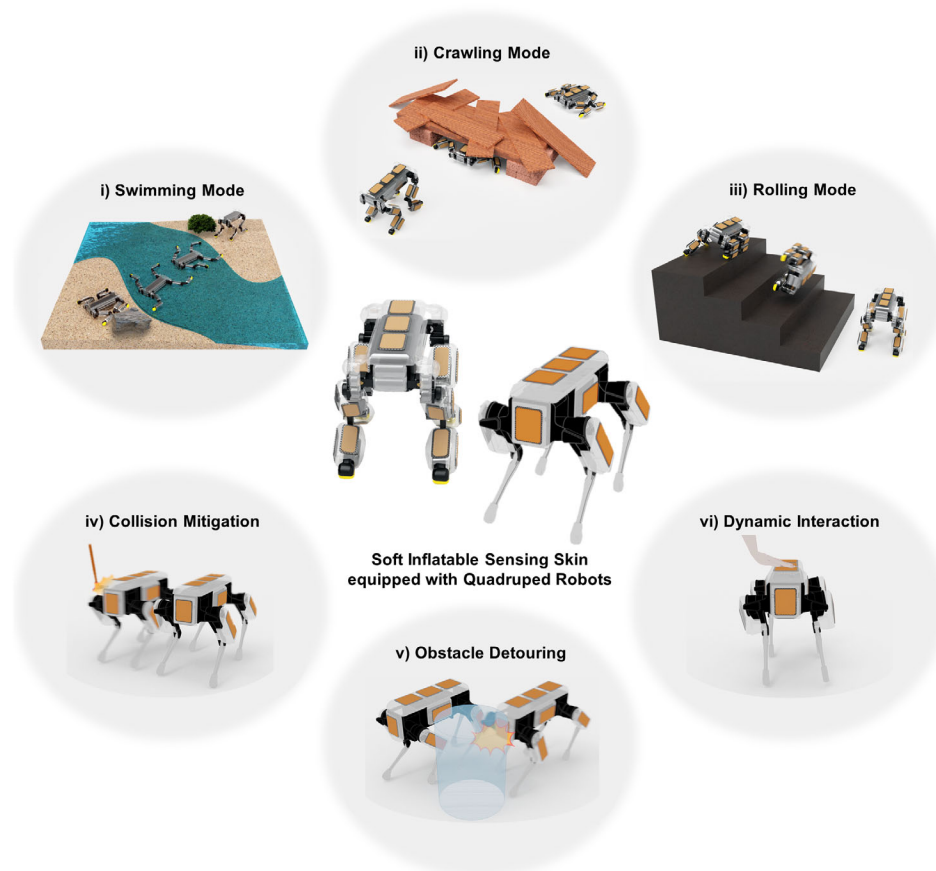

Figure 1. Multimode locomotion and environmentally adaptive responses enabled by cutaneous inflation and tactile sensation. i) Floating and swimming with buoyancy and propulsion, ii) crawling with stable ground contact and friction, iii) rolling down from height with air cushions, iv) impact detection and mitigation, v) obstacle recognition and detouring, and vi) dynamic whole-body interaction with surrounding.
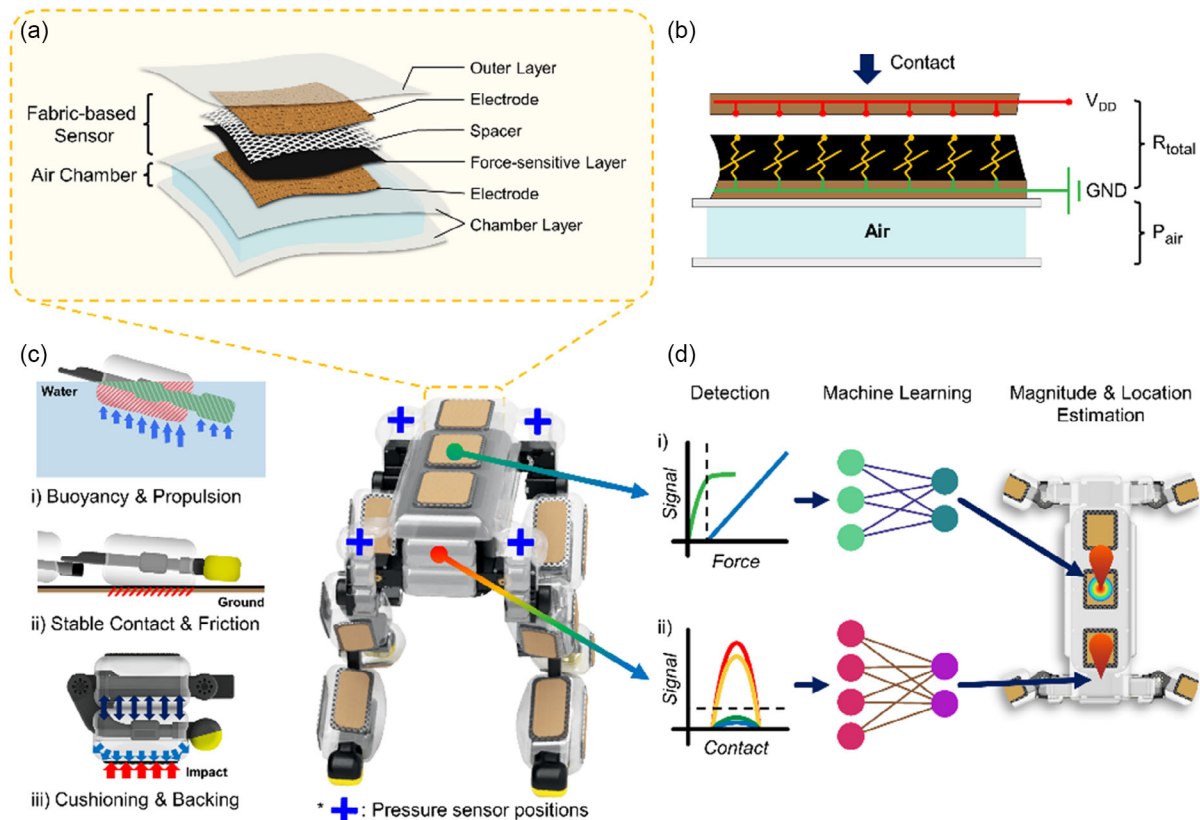
**ADVANCED
SCIENCE NEWS**

www.advancedsciencenews.com

**ADVANCED
INTELLIGENT
SYSTEMS**
Open Access

www.advintellsyst.com

Figure 2. Design and functionalities of the soft inflatable sensing skin. a) Structural design of the inflatable sensing skin. b) Schematic illustration of the tactile sensing structure. c) Functionality of the inflated skin based on its structural properties: i) sufficient buoyancy and propulsion on the water, ii) stable contact and friction force with the ground, and iii) cushioning and backing effects from physical impact. d) Tactile sensing functionalities: contact i) magnitude and ii) location estimation using machine learning.

3D robot structures was difficult and time consuming. To address this, they proposed a lightweight inflatable sensing skin composed of thermoplastic sheet layers that contained fabric-based capacitive touch-sensitive pads and an air pressure sensor.[55] This reduced the weight significantly compared to the silicone skin, and fabrication was simplified by using a heat-sealing process. However, the capacitive touchpad could only detect contact as binary states, and it was impossible to measure the magnitudes of pressures applied on each contact location using a single air pressure sensor.

In this research, we improve the sensing performance of the inflatable skin by incorporating a conductive fabric-based resistive sensing structure that directly measures the contact force magnitude. Previous works[54,55] focused solely on human–robot interactions for safety purposes through inflatables integrated with a single robotic arm or leg. However, we demonstrate the potential of inflatables covering the whole body of a quadruped robot to enhance its functionalities and stability by providing additional environmental adaptability. We validate this through successful implementation of dynamic human–robot–environment interaction scenarios.

In addition, there have been some efforts to enhance legged-robot locomotion using tactile information in unstructured terrains without vision sensors. Mobile robots commonly rely on light detection and ranging (LiDAR) sensors and cameras.[56,57] These sensors help robots obtain essential information to recognize surrounding landforms and risk factors, such as obstacles and collisions. However, LiDAR is unable to detect objects outside of its horizontal, vertical, and distance fields of view. LiDAR also requires computationally expensive signal processing and is vulnerable to optical effects, such as blooming. Cameras face challenges in blind spots and in low-light environments. In such situations, tactile sensing can provide intuitive information, especially in unstructured terrains. Luneckas et al. demonstrated a hexapod robot overcoming complex obstacles based only on the use of tactile sensors attached to its legs.[58] Mrva et al. proposed a hexapod robot that only utilized the torque and position outputs of servo motors at the joints to estimate the contact points of obstacles without extrinsic tactile sensing.[59] While most studies on the tactile sensing capability have focused on overcoming unstructured environments with obstacles, our study using soft inflatable sensing skin additionally demonstrates the potential for better impact mitigation and dynamic human–robot–environment whole-body interaction by accurately estimating force magnitude and location.

Using various structural properties and tactile information, our inflatable robotic sensing skin synergistically works with the host robot to implement additional mobility and enhance

self-defense, autonomy, and interaction with environments. It offers buoyancy and volumed forms, which allow for swimming and crawling (Figure 1i(ii)). In addition, previously difficult tasks, such as descending from large-height structures, are now possible through rolling down (Figure 1(iii)) using cushioning and backing protection effects of the inflated skin. This additional mobility allows the host robot to enlarge its operating domain with simple control methods. Furthermore, the tactile sensors integrated with the inflatable skin enable the host robot to take actions quickly and accurately to defend itself and adapt in risky situations (Figure 1(iv) and 1(v)). The tactile sensors are also used to estimate the magnitudes of external forces and infer their intentions, allowing the robot to interact with the environment more dynamically (Figure 1(vi)).

We verify the effects of the proposed inflatable sensing skin by equipping it to both a custom-built quadruped robot and a commercial quadruped robot (Figure S1–S5, Supporting Information). The custom-built robot with the inflated skin was able to display unique mobilities that had been previously difficult for conventional quadruped robots. We then integrated the skin with a commercial robot to demonstrate that the skin can be universally applied to any quadruped robot. The commercial robot was used to show application scenarios in which the tactile sensing capability enhances safety, autonomy, and interaction.

2. Results

2.1. Enhanced Mobility Using Cutaneous Inflation

2.1.1. Floating and Swimming with Buoyancy

The development of legged robots has focused on robust walking to enlarge the operable area on land.[9,11,13–15,21,24–30,34,36–39] However, for legged robots to be useful in various environments, they must also be able to operate under aquatic conditions. Various groups have conducted research on legged robots with unique leg designs for operation in aquatic environments[60–67] but have had difficulty achieving high amphibious maneuverability. Furthermore, unique design factors for swimming, such as the position of leg joints, make it difficult to apply common controllers for the latest quadruped robots, such as ANYmal, Spot, and Cheetah.[48,61,67] Other groups have developed robots that walk underwater.[63,64] However, these robots required robust waterproofing measures depending on the depth of the water. Robots that operate underwater face depth-related problems, such as communication delay and high water pressure. In contrast, legged robots that can float and swim on water are more versatile and efficient across various landforms while reducing water-related problems.

To extend operation to aquatic environments, we implemented swimming capabilities for the custom-built legged robot using the inflated skin. The skin to cover the whole body of the custom-built quadruped robot has a light weight of approximately 400 g and a relatively large volume of approximately 5.14 L when inflated. Therefore, when the inflated skin is integrated with the custom-built quadruped robot, it makes the average density of the robotic system (from 1.32 to 0.58 g cm^{-3})

much lower than that of water (1 g cm^{-3}), allowing it to stably float (**Figure 3**a). The total weight of the robot equipped with the inflated skin is approximately 4.94 kg, and it is expected that the robot will occupy a submerged volume of approximately 4.94 L.

We planned the robot leg forward movement and rotation swimming trajectories based on the submergence depth of the robot's body. To swim forward, the robot starts by pushing its underwater legs toward its back, as shown in Figure 3b and S6a, Supporting Information. This creates drag forces, propelling the robot forward. Then, the robot lifts its legs above the water surface and moves them forward to return to their underwater starting position. When rotating, only one front leg generates a drag force, while the other legs are stretched to minimize rollover, as shown in Figure S6b and S6c, Supporting Information.

Furthermore, during the swimming motions, since the inflated skin has an effective cross-sectional area 3.88 times larger in water than that of the bare leg frame, the inflated skin generates sufficient propulsion with larger drag forces (Figure 3c). This improves the swimming efficiency. Figure 3d shows collected propulsion forces during the forward swimming motion using a test setup with a pair of the front legs (see more details in Note S1, Figure S7a, and Video S1, Supporting Information). With the inflated skin, the maximum force was 1.22 times larger than that in the case without the inflated skin, resulting in dragging the leg structures forward 1.68 (dW_w/dW_{wo}) times further on the water (Figure 3d). This result confirms that the increased effective cross-sectional area by the inflated skin enables the planned swimming motion to generate propulsion more efficiently.

To validate the swimming performance in the real environment, the robot was placed in a stream (see Video S1, Supporting Information). The robot crawled from the bank into the water and swam to the target points. The robot successfully passed the target points by appropriately swimming forward and rotating. Last, it crawled out of the water at the end of the course. The path and target points are shown in Figure 3e. The swimming stability was also demonstrated through long-distance swimming of approximately 85 m over 7 min (Figure S8 and see Video S1, Supporting Information).

2.1.2. Crawling with Stable Ground Contact and Friction

In unstructured environments, such as disaster sites, there exist not only uneven terrain but also low-ceiling structures that can only be passed by adjusting the height of mobile robots.[15,68,69] For most quadruped robots to pass through such a scenario, they create a gait motion while lowering their body height.[15] In this posture, the moment arm formed by the robot's leg links increases with respect to the rotational axis of each joint. Therefore, the joint torque generated to support the robot's body-weight becomes significantly large, and more power is required to create the gait motion while withstanding this load, limiting the robot's range and speed of motion. In addition, the gait in this posture cannot make a minimum height equal to the robot's body height because it needs enough space underneath the body for the leg motions, making the robot more easily unstable on the uneven terrain.
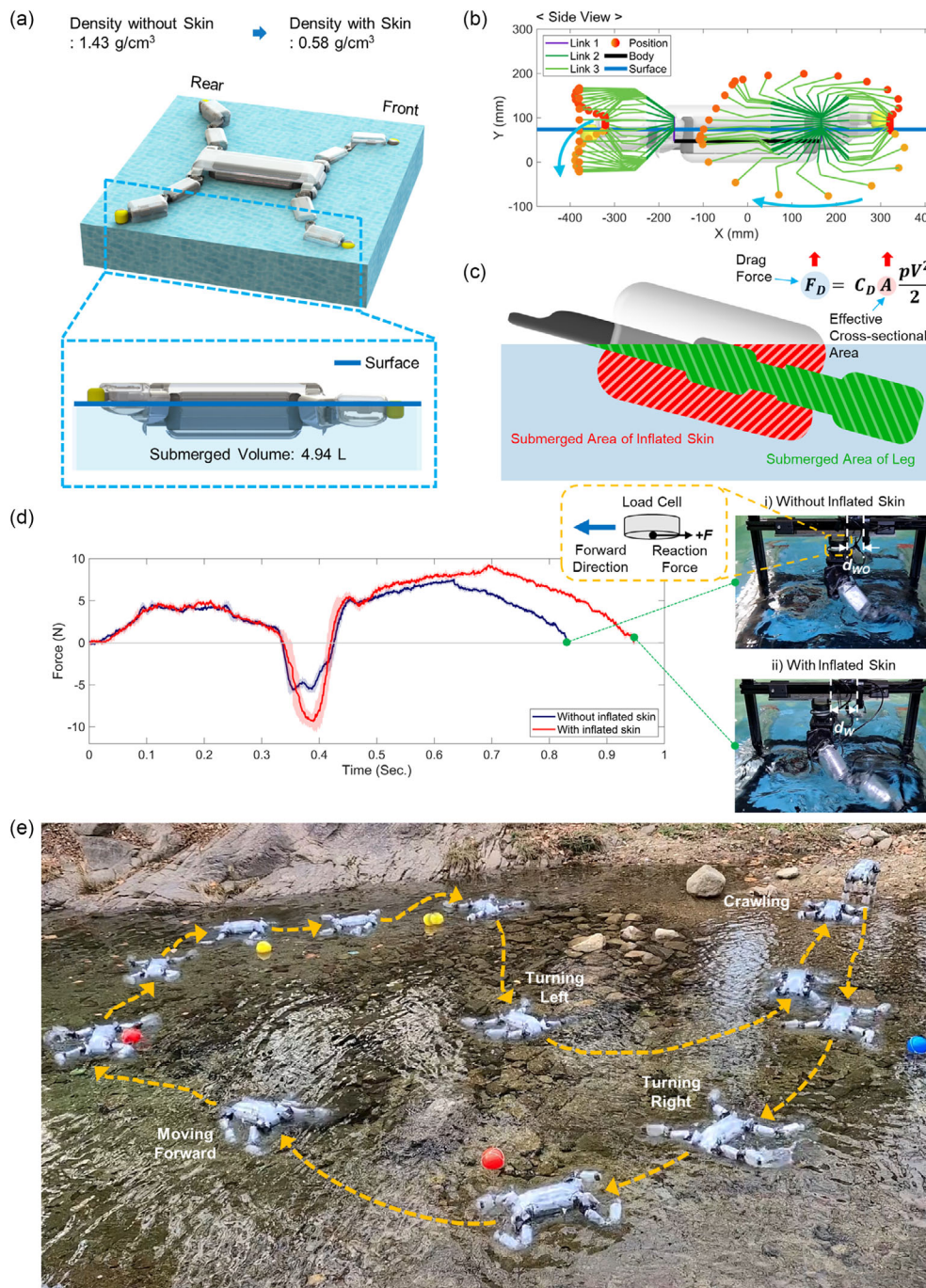
Figure 3. Floating and swimming on water environments. a) View of the custom-quadruped robot floating on the water. Inset shows the side view of the floating robot with a submerged volume of 4.94 L. b) Leg trajectories for the forward swimming motion. The black line represents the robot body. The purple, dark green, and light green lines represent the first, second and third leg links from the body, respectively. The blue line shows the surface of the water, and the yellow and red dots represent the tip of the distal leg link (the third leg from the body). The light blue arrows indicate the direction of the drag force. Figure S6A,B, Supporting Information show a top view of the leg trajectories for the forward swimming motion and leg trajectories for the rotation-swimming motion, respectively. c) Cross section of the submerged area of the leg. The green and red diagonal lines represent the submerged area of the leg and the inflated skin, respectively. d) Reaction (propulsion) forces measured by the loadcell while the robotic legs paddle the water with or without the inflated skin in swimming motions (d_w: the maximum distance dragged by the swimming motion with the inflated skin, d_{wo}: the maximum distance dragged by the swimming motion without the inflated skin). e) Snapshots of the swimming test in a real environment. The yellow dashed line shows the path of the robot. The yellow, red, and blue buoys are the target points of the swimming scenario.

**ADVANCED
SCIENCE NEWS**

www.advancedsciencenews.com

**ADVANCED
INTELLIGENT
SYSTEMS**
Open Access

www.advintellsyst.com

We propose another type of stable crawling motion to address these limitations by taking advantage of the volumed form and compliance of the inflated skin. To create this motion, the body structure first makes direct contact with the ground by letting the legs spread out to the side. This removes the load on the motor required for supporting the body weight and makes the legs move freely, enabling the robot to respond more actively to changes in the surrounding environment. While the robot is in this basic posture, the volumed form of the inflated leg skin provides a wide contact area with the ground (**Figure** 4a). In addition, the skin's compliance allows for stable contacts to be made with various types of surfaces. Therefore, a stable and sufficient friction force between the leg skin and the ground allows the robot to drag its body across the floor, creating an efficient and flexible crawling motion.

The forward crawling motion is generated by dragging across the ground with the inflated skin of all the distal legs. For this motion, the leg trajectory is implemented to increase the contact surface area of the inflated skin while considering the volumed form of the skin, as shown in Figure 4b and S6d, Supporting Information. Before the horizontal movement of the legs, the vertical movement of the legs slightly lifts the robot's body to minimize the friction with the ground and to maximize the normal force applied by the inflated skin to the ground. Then, the horizontal movement of the legs drags the body of the robot. Rotation while crawling is realized by generating the same type of forward motion trajectory using only two legs on one side of the robot's body. In Figure S9a and S9b, Supporting Information, the sensing signals from the fabric sensors facing toward the ground also demonstrate that stable ground contact is developed during the forward and rotation crawling motions, respectively.

Figure 4c shows the contact force (Figure 4c-left) and distribution (Figure 4c-right) measured by a test setup using a single robotic leg during the entire crawling motion with and without the inflated skin (see more details in Note S2, Figure S7b, and Video S2, Supporting Information). With the inflated skin, the contact points with the ground were more concentrated in adjacent areas and the area was 1.35 times wider while the magnitudes of the contact forces were even 1.94 times lower than those in the case without the inflated skin. However, despite the lower contact forces, the reaction forces collected by the loadcell were 1.68 times larger than those without the inflated skin (Figure 4d-left), resulting in dragging the single leg structure 2.31 ($dW_{\mathrm{w}}/dW_{\mathrm{wo}}$) times farther as shown in Figure 4d-right. Therefore, this result confirms that the inflated skin enables the crawling motion to be efficient.

By combining forward and rotation crawling motions, we carried out a test in which the custom-designed quadruped robot passed through a low-ceiling structure with a height of 250 mm (see Video S2, Supporting Information). The robot in the standing state first changed its posture in preparation for the crawling motions (Figure 4e(i),(ii)) and then rotated while crawling to turn toward a path without any interference from obstacles (Figure 4e(iii)). After that, the robot crawled straight under the structure (Figure 4e(iv)) and rotated again to avoid collisions with the structure (Figure 4e(v)). Finally, the robot crawled out from the structure (Figure 4e(vi)). Figure S10, Supporting Information shows the output signals of the fabric sensors in contact with the ground during the presented course of action.

2.1.3. Rolling Down from Heights with Air Cushions

Ascending or descending slopes is one of the most challenging tasks for mobile robots.[70,71] Existing slope-climbing robots involve modifications of the locomotive mechanism form factors, such as shape-adaptive tracks or transformable wheels.[70–73] In the case of legged robots, more complex control methods based on highly accurate vision information must be implemented to ascend and descend staircase slopes.[26,74,75] Descending a slope is generally a more challenging task than ascending a slope since it requires more sophisticated control to avoid losing robot's balance. Furthermore, there is a fundamental physical limit on the height of the structure that a legged robot is able to descend based on general gait motions available to the robot's hardware.

This study presents a solution in which the protective effects of the inflated skin in a structurally safe posture (**Figure 5**a) allow legged robots to descend from slopes easily and safely with a large height without complex control strategies. The inflated skin provides two types of protective effects, a cushioning effect and a backing effect. The cushioning effect refers to reducing the impact by increasing the damping coefficient in a collision. The backing effect refers to reducing the structural deformation through the presence of supporting forces between rigid robot bodies. The protective effects of the inflated skin are demonstrated through two types of collision tests. One is a single-leg collision test, and the other is a whole-body collision test (see more details in Note S3, Figure S11–S13, and Video S3, Supporting Information).

The single-leg collision tests were conducted in two cases: free falling on a force plate and collision with an external object (see more details in Note S3, Figure S11a,b, and S12, Supporting Information). Figure 5b shows the mean and standard deviation of knee joint torque with or without the inflated skin by the free falling. In the absence of the inflated skin, the maximum torque was 6.05 N m. With the inflated skin, the maximum torque was 2.58 N m, 57% smaller than the maximum impact torque without the skin. These results confirm that the backing effect between the two inflated chambers installed on the proximal, and distal links can prevent harmful joint torque, which is useful in preventing damage of the motor. The cushioning effect of the inflated skin is leveraged to distribute the impact, by inducing more bounces of the robotic leg, which results in a 31% smaller peak impact force (Figure 5c). The peak force is 175.34 N without the inflated skin and 120.88 N with the inflated skin. Figure 5d shows the results of the collision test by an external object. The inflated skin can reduce the peak impact force (50.95 N) by 48% compared to the peak impact force (99.31 N) without the skin. For the whole-body collision test, only the free-fall test was conducted since the result of the external object collision test is expected to be similar to that performed on a single leg. Note 3, Figure S11c, and S13, Supporting Information present detailed analysis and results.

Our custom-designed quadruped robot was able to descend a staircase slope with a large step height through rolling (see Video S4, Supporting Information). Since the stairs shown in Figure 5e
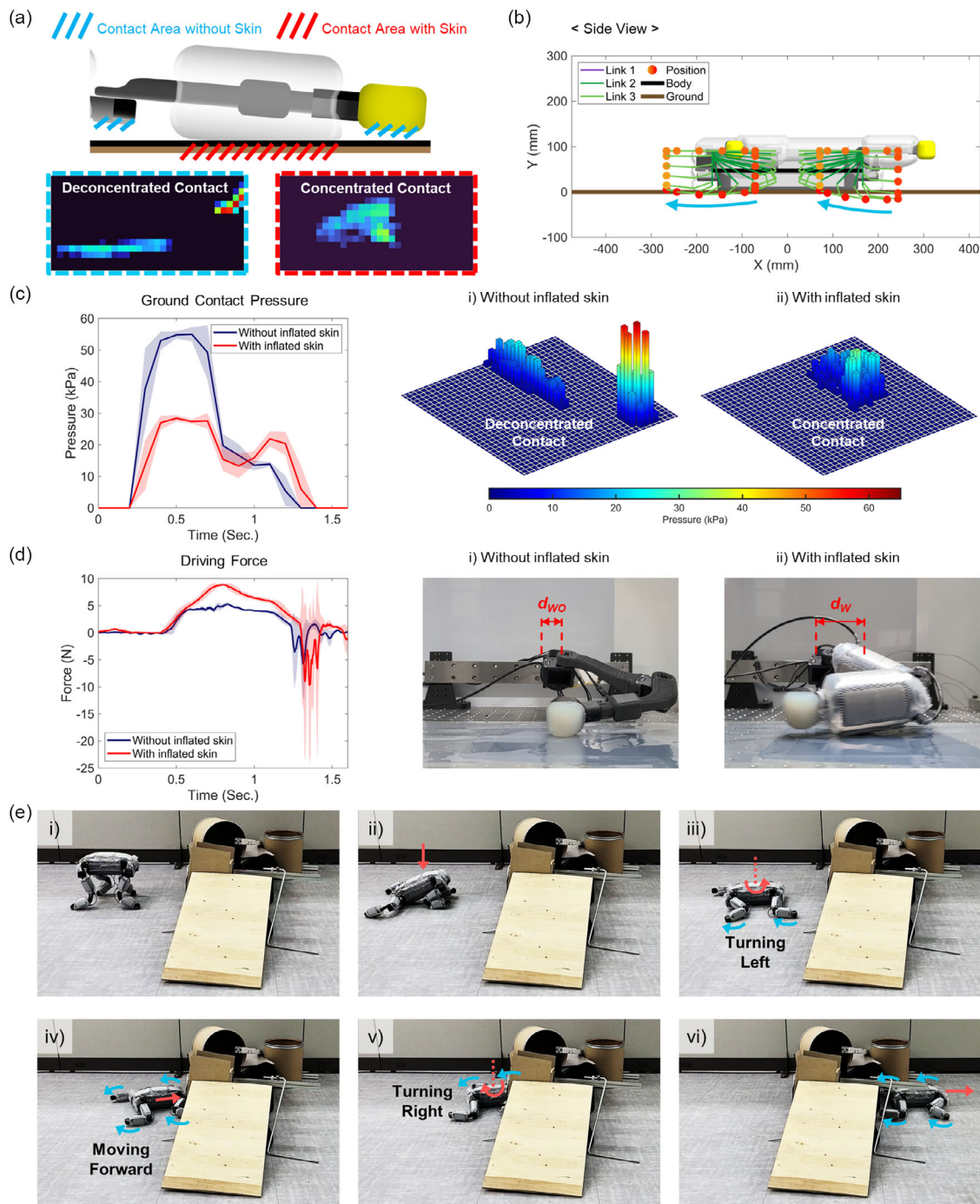
222

Figure 4. Crawling through confined space. a) Contact with the ground in cases with and without the inflated skin. Insets show the contact area with (right) and without (left) the skin. b) Leg trajectories for the crawling motion. The black line represents the robot body. The purple, dark green, and light green lines represent the first, second, and third leg links from the body, respectively. The brown line shows the ground, and the yellow and red dots show the center of the distal leg link (the third leg from the body). A top view is depicted in Figure S6d, Supporting Information. c) Maximum ground contact pressures measured by the force pad while the crawling motion with or without the inflated skin (left) and ground contact pressure distributions measured by the force pad while the entire crawling motion (i) with or (ii) without the inflated skin. d) Reaction forces measured by the loadcell by dragging the ground in the crawling motion (left) and maximum dragged distances by the crawling motions (i) with or (ii) without the inflated skin (d_w: the maximum distance with the inflated skin, d_{wo}: the maximum distance without the inflated skin). e) Snapshots of the crawling scenario: i) starting posture, ii) sitting down in preparation for crawling, iii) right-turn crawling motion, iv) forward crawling motion, v) left-turn crawling motion, and vi) forward crawling motion to arrive at target point.
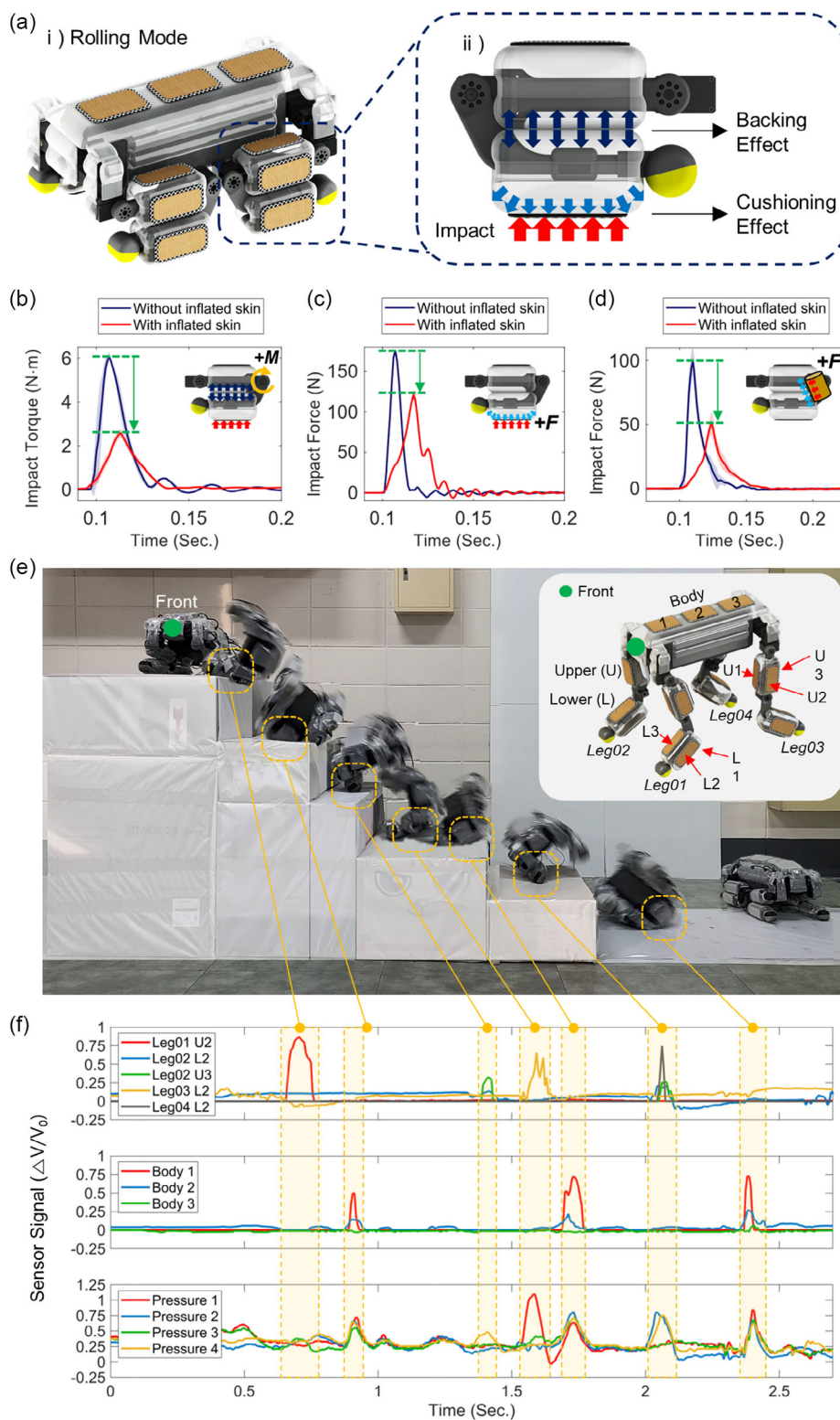
2300172 (7 of 16)

Figure 5. Rolling down from a steep stair-like structure. a) Safety effects (backing and cushioning) in the rolling mode. b) First impact torque results in the single-leg free-fall test. c) First impact force results in the single-leg free-fall test. d) First impact force results in the collision test with an external object. e) Setup of the staircase and snapshots of the robot while rolling down. The subfigure on the right shows how each sensor was labeled. f) Outputs of the fabric and pressure sensors during rolling down the stair-like structure.

**ADVANCED
SCIENCE NEWS**

www.advancedsciencenews.com

**ADVANCED
INTELLIGENT
SYSTEMS**
Open Access

www.advintellsyst.com

have maximum and minimum step heights of 306 and 191 mm, respectively, it is impossible for a quadruped robot with a maximum body height of 300 mm to descend using general gait motions. However, by rolling in a crouched posture, the robot was able to safely descend the structure (Figure 5e). This result confirms that the inflated skin successfully protected the robot from several collisions while rolling down. The skin's ability to reduce the excessive torque externally applied and harmful to the joints and to alleviate structural deformation allowed the robot to decrease damage to the motors. Moreover, the inflated skin prevented stress concentration, which helped to block physical damage to the robot hardware. Furthermore, the robot equipped with the inflated skin was able to bounce after each collision with a forward momentum sufficient to keep the rolling motion to descend stairs to the end without stopping. In addition, Figure 5f shows the tactile sensing signals from the fabric and the air pressure sensors caused by multiple collisions, which are useful in estimating the collision locations during descent.

2.2. Enhanced Adaptability to Surroundings Using Cutaneous Sensation

The proposed inflatable skin obtains tactile information using two different types of sensors: one is fabric-based touch sensors attached to the surfaces of the inflatable skin; the other is air pressure sensors connected to the air chambers. According to the characterization results (**Figure 6**a–c and see more details in Note S4, Figure S14–S16, and Video S5, Supporting Information), the two sensor types have different sensing characteristics that are complementary to each other. In the low force range (under 2.5 N), the high sensitivity and linearity of the fabric sensors can compensate for the insensitivity of the air pressure sensors. After the low force range, the linear and sensitive sensing signal of the air pressure sensors supplements the saturated and highly nonlinear fabric sensor signal. Therefore, the fabric and air pressure sensors complement each other in terms of sensitivity and linearity. Tables S1 and S2, Supporting Information summarize the nonlinearity, error, and sensitivity of each loading and unloading force range from 0 N to 2.5 N and from 2.5 N to 31 N, respectively.

2.2.1. Impact Detection and Mitigation

We implemented impact mitigation scenarios in which the quadruped robot detected impacts with tactile information from a fabric-based touch sensor (see Video S6, Supporting Information). Most commercial quadruped robots already possess embedded control strategies to maintain stability and balance from external disturbances. For example, impedance control and disturbance observer-based control enable robots to endure disturbances and maintain stable postures.[76–80] However, these control methods are inadequate when robots rapidly lose their balance due to a large impact force. Some quadruped robots recognize imbalances using sensors, such as IMUs and foot pressure sensors, and then move to a new capture point (CP) through compensatory walking steps.[47,81–86] However,

these control methods only respond after stability is broken, and the reaction may be too slow.

On the other hand, tactile sensors can be used to provide intuitive information to the controller. By accurately and immediately measuring small contact forces through fabric sensors, they allow the robot to respond quickly to impacts. A short response time allows the robot to perform mitigative behaviors before losing its balance and reaching its hardware limit. To demonstrate these benefits, we conducted two experiments in which impacts were applied to the quadruped robot using a robotic arm (UR3, Universal Robots), as shown in Figure 6d. In both scenarios, the quadruped robot utilized the same controller, which prioritized the emergency restoration of the robot's body balance (Figure S4b, Supporting Information). Additionally, the robot's functionality was enhanced by incorporating a mitigation action based on signals from tactile sensors. Whenever the sensor signals surpassed a predetermined threshold, the leading PC issued commands to the robot, directing it to walk in the opposite direction of the impact, such as executing a side step. This behavior is depicted in Figure S4b and S4c, Supporting Information. The two experiments were for the impacts applied to a leg equipped with and without the inflated sensing skin.

The test results are shown in Figure 6d and S17 and S18, Supporting Information. The robot with the inflatable sensing skin reacted approximately 2.88 times faster than the robot without the skin. This result demonstrates that the fabric-based tactile sensor allowed the robot to mitigate impacts within a shorter response time and avoid detrimental situations, such as falling down or losing balance. The fabric sensor in the inflatable skin was able to detect low force impacts (up to 2.5 N) without any buffer effect. However, the initial impact was still noticeable despite the presence of a buffer effect from air dynamics within the inflated chamber. This was overcome through the combined use of two sensing mechanisms within the skin. The robot with the inflatable skin received an approximately 33% smaller peak impact force resulting from the short response time and from the damping and cushioning effects. In addition, both the maximum side velocity and the change in the first case were smaller than those in the second case. These results indicate that a robot with tactile sensing is able to safely adapt and maintain better stability during impact. This can also be inferred from the changes in the foot contact forces and the z-axis foot position of each leg, as shown in Figure S17, Supporting Information. As the robot took compensatory steps to the side, the foot contact force changed more significantly in the second case than in the first case. This shows that the tactile sensing allows the robot to take an earlier evasive reaction so that the load from the impact can be mitigated, ensuring the robot's stability. To demonstrate the effect of the tactile sensing more clearly, we conducted an additional test in which an impact was applied to the skin with the sensors disconnected (Figure S19, Supporting Information). In this case, only the maximum impact force was decreased by damping and cushioning. The maximum velocity, the change in the foot contact force, and the change in the z-axis foot position were similar to those of the robot without the inflated sensing skin, as shown in Figure S18, Supporting Information. This means that the tactile sensing plays a more important role in managing impacts than the cushioning effect does.
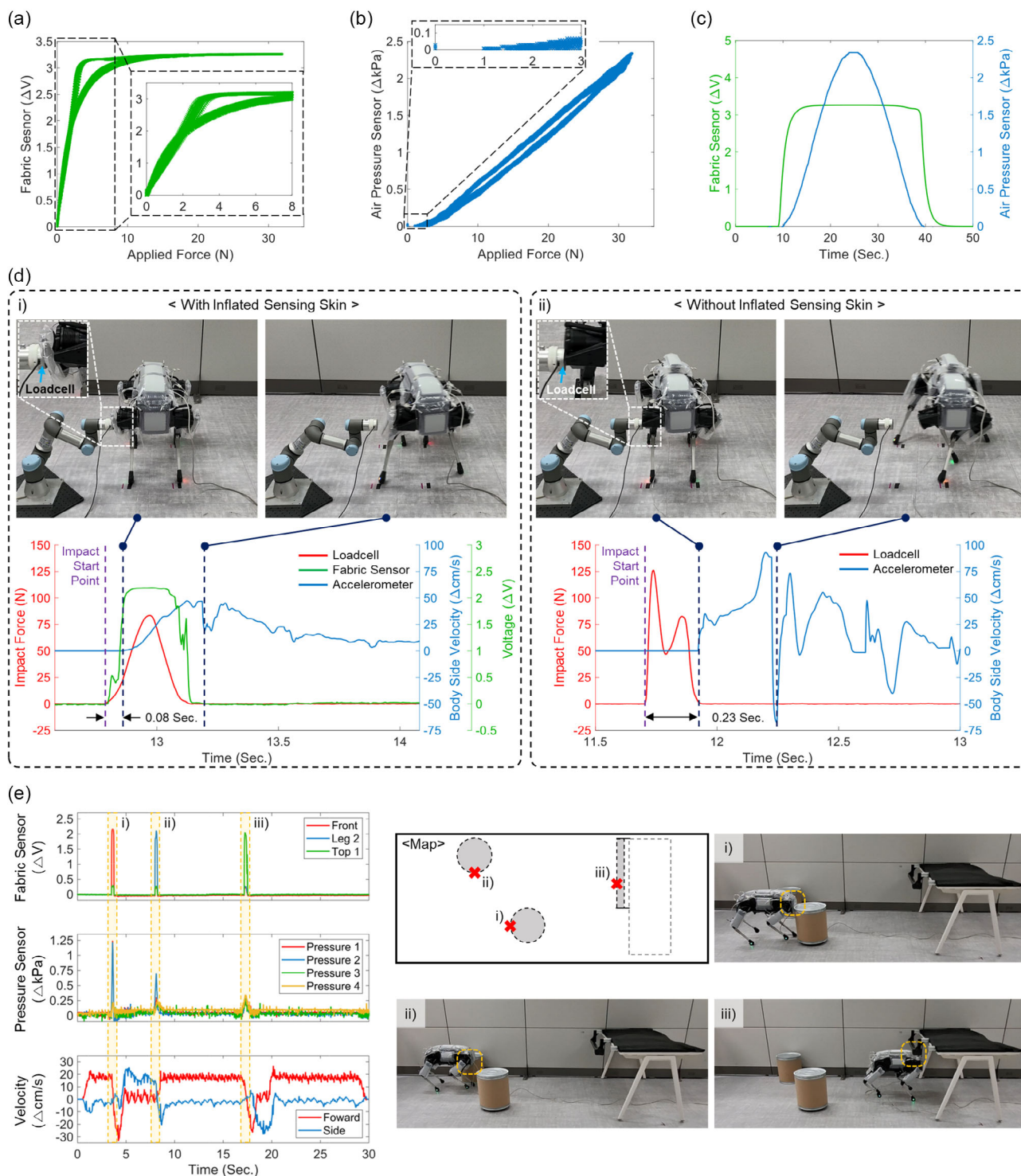
ADVANCED
SCIENCE NEWS
www.advancedsciencenews.com

ADVANCED
INTELLIGENT
SYSTEMS
Open Access

www.advintellsyst.com

Figure 6. Enhanced safety and autonomy using tactile sensation. a) Fabric-based touch sensor output. b) Air pressure sensor output. c) Comparison of the outputs from the fabric and the air pressure sensors during one cycle. d) Reactions of impact with and without inflated sensing skin: i) Results due to impact forces, fabric sensing data, and robot moving velocity when the impact force is applied to the inflatable sensing skin. The purple dashed line shows the time when the impact starts, and the first navy line shows the time when the robot starts to respond. The tactile sensor signal allows the robot control to respond in a shorter timeframe (0.08 s). ii) Results due to impact forces and robot body moving speed when the impact force is applied without the sensing skin. e) Sensor outputs (left) and snapshots (right) of collisions applied to various parts of the robot: i) head collision, ii) side leg collision, and iii) top body collision. The left figure shows fabric and air pressure sensor signals and the robot velocity. The right figure shows the map and snapshots of each collision.

2.2.2. Obstacle Recognition and Detouring

We also implemented a scenario to demonstrate the obstacle avoidance ability of a robot equipped with the proposed skin (see Video S7, Supporting Information). When physical contact occurs, the robot uses its fabric-based touch sensors to recognize obstacles and correct its path. More specifically, when the sensors on the front and top of the robot detect obstacles, the robot goes back a few steps and moves sideways to detour the obstacles. When the sensors on the side of the robot detect obstacles, the robot moves in the opposite direction of the contacts.

Figure 6e shows the test environment with obstacles. The first obstacle caused a head-on collision with the robot, and the robot moved backward to avoid the obstacle, as shown in Figure 6e(i). Then, the robot detoured to the left and collided with the second obstacle, as shown in Figure 6e(ii). Next, the robot moved slightly to the right and passed between the two obstacles. Finally, when the head of the robot was in contact with the third obstacle, as shown in Figure 6e(iii), the robot slightly moved back and arrived at the target line by detouring to the right.

2.2.3. Dynamic Interaction with Surroundings

The tactile sensing plays an important role not only in the perception of the surrounding environment and the assessment of risk factors but also in the interaction with humans or other robots. In other words, the robotic skin with tactile sensors enables a quadruped robot to collaborate better with humans or other robots. In particular, when a robot threatens the safety of people around it or even itself, it can physically and intuitively control the robot to escape from emergencies since the tactile sensors can serve as control touchpads to directly guide the robot's motion or posture. Furthermore, the robot can logically infer the intention and choose appropriate reactions, such as physical interaction or evasion, by estimating the magnitudes or directions of contact forces using the tactile sensors. Therefore, tactile sensing increases environmental adaptability in a wide variety of situations. To demonstrate this capability, we implemented three test cases. In the first case, the quadruped robot inferred the intention of the contacts and reacted differently according to the types of forces. In the second case, an operator guided the robot by touching the tactile sensors on the skin. In the third case, the quadruped robot physically interacted with a commercial robotic arm while maintaining a target level of contact force with the robotic arm.

For the first case, the quadruped robot classified the applied forces as either friendly or harmful contacts using the skin fabric sensor based on the threshold force level (see Video S8, Supporting Information). When the applied force was lower than the threshold, the applied force was classified as interactive touch, and the robot rotated slightly clockwise then counterclockwise about the yaw axis, as shown in **Figure 7**a(i). When the applied force was higher than the threshold, it was classified as destructive impact, and the robot avoided the impact by pivoting forward, as shown in Figure 7a(ii). This case demonstrates that the skin can be used to determine the intention of external forces and appropriately respond to them.

In the second case, the fabric sensors located on various parts of the body were used as control pads to allow human touches to guide the quadruped robot (see Figure S20 and Video S9, Supporting Information). The robot changed its posture, moved, or rotated based on the contact location. The three fabric sensors at the top of the body were used to change the posture while standing. For example, when a human operator touched the center pad, the robot lowered its body height. When the front or rear pad was touched, the robot changed the height and pitch angle simultaneously, as shown in Figure S21a(i),(ii), Supporting Information. The robot rotated to avoid contact when touched on the leg, as depicted in Figure S21a(iii),(iv), Supporting Information. When the front, rear, or side was touched while walking, the robot moved in the opposite direction of the contact, as shown in Figure S21b(i),(ii), Supporting Information. Figure S21b(iii),(iv), Supporting Information illustrate the angular acceleration about the yaw-axis of the robot when it avoided a touch to the leg. This case shows that a robot with the sensing skin interacts more fluidly with humans by interpreting the operator's physical contacts as commands.

As shown in the previous scenario, basic contact localization was possible in discrete areas where the fabric sensors are embedded by placing the fabric sensors to cover as much of the skin surface as possible to maximize contact localization capability. However, fabric sensor dead zones, the areas that are not covered by the sensors, exist on small and curved areas of the skin. When external forces are applied to the dead zones, only the air pressure sensors provide meaningful signals. Therefore, we used artificial neural network (ANN)-based machine learning to approximately localize the contacts only from the air pressure sensor data (Figure 2d(ii) and see more details in Note S5 and Figure S22a, Supporting Information). Figure S23a, Supporting Information shows different output patterns of the air pressure sensors depending on the location of the applied external force. In general, when a force is applied to a leg, the air pressure sensor closest to the leg measures the largest increase in pressure. When an external force is applied to the body, all the air pressure sensors respond simultaneously. As shown in Figure S23b, Supporting Information, the ANN-based model was able to successfully localize the contacts among five areas (one body and four legs, Figure S24, Supporting Information) from only the air pressure data, with high accuracies of more than 94%. This demonstrates that contact localization is possible through the use of air pressure sensors and an ANN, despite the unavoidable fabric sensor dead zones. Furthermore, the ANN model trained the nonlinear effect of the delay between the impact and the response from the buffer effect of the air chamber.

In addition, calibrating using ANN-based machine learning can take advantage of the compensatory relationship of outputs from fabric and air pressure sensors to efficiently extend the range of tactile force sensing and to estimate the contact force magnitude more accurately (Figure 2d(i) and see more details in Note S5 and Figure S22b, Supporting Information). When a network was trained using both fabric and air pressure sensor data, the root-mean-square errors (RMSEs) were 0.75 N and 0.47 N in the loading and unloading phases, respectively. The accuracy was higher than those of cases where a network was trained with only fabric or only air pressure sensor data
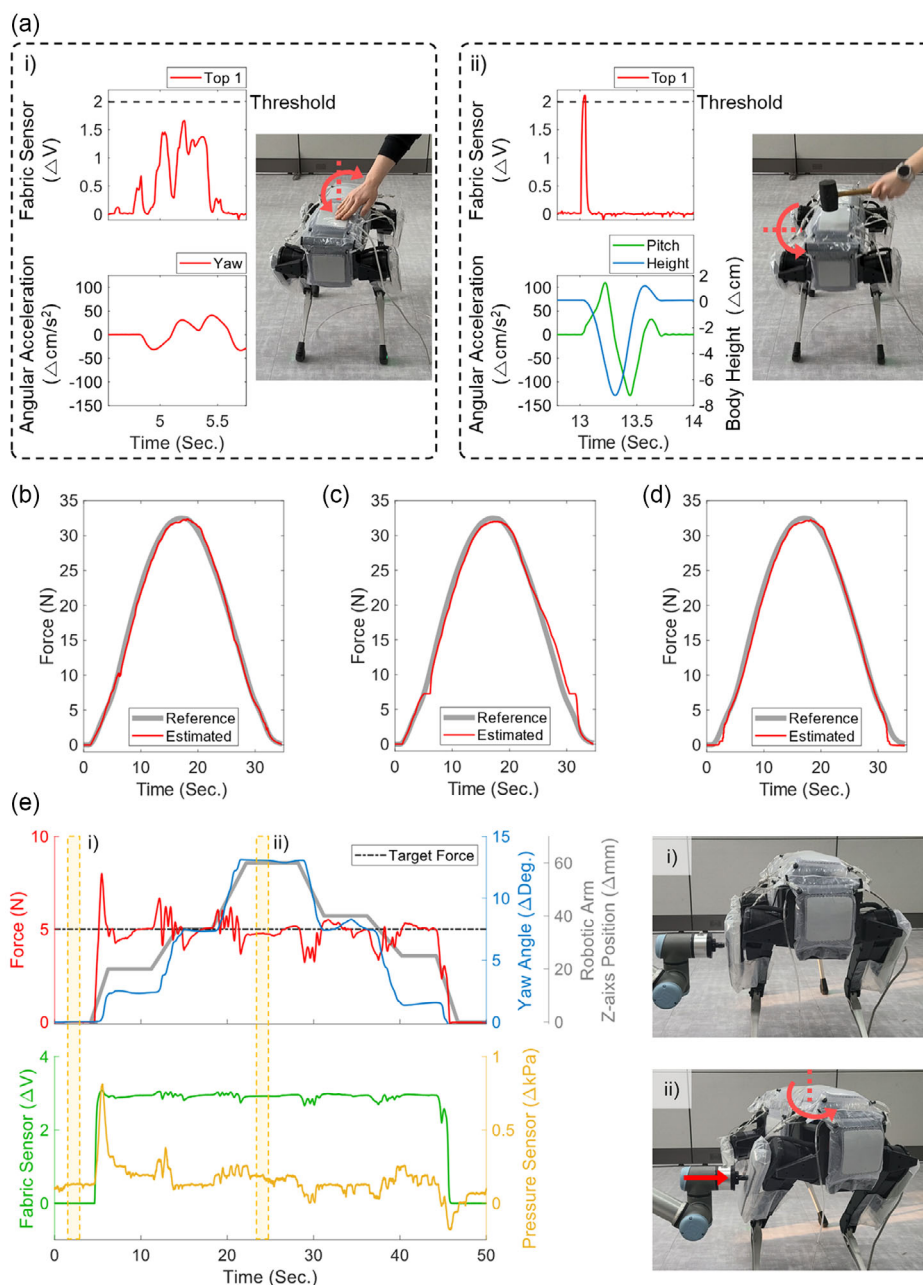
Figure 7. Dynamic interaction with surroundings. a) Classification of external force intention: i) the external force is under the threshold, and the robot creates a friendly interactive motion, ii) the external force is above the threshold and is classified as harmful. The robot creates a motion to mitigate damage. Force estimation results with b) both fabric and air pressure sensor datasets, c) only the fabric sensor dataset, and d) only the air pressure sensor dataset; and e) interaction with a robotic arm. The yaw angle of the quadruped robot was controlled to maintain a constant force (5 N) with the robotic arm.

over the entire range of force magnitudes, as shown in Figure 7b–d (see more details in Note S6 and Table S3, Supporting Information summarizes the RMSEs of each calibration case).

Therefore, in the third case, the tactile sensors were first calibrated with an ANN-based machine learning method (see Video S10, Supporting Information). The calibration result is shown in Figure S25, Supporting Information, and the RMSE of the

estimated force was approximately 0.79 N. According to the horizontal displacement of the interacting robotic arm, the quadruped robot rotated its body about its yaw axis. To maintain the target contact force of 5 N, a simple proportional-integral-differential (PID) controller was implemented to the robot. The PID controller was used to derive the trajectory of the yaw angle of the robot so that it maintained the target force without losing its stability, as shown in Figure 7e (see Video S10,

Supporting Information). This case shows that the estimation of the contact force helps the robot interact safely with other robots.

3. Conclusion and Future Work

This study presents a synergistic combination of two recently advanced technologies: inflatable sensing skin and legged robots. Although existing legged robots are already highly advanced using stable control methods, high-power actuators, and accurate optical sensing, the inflatable sensing skin can be easily applied to any legged robot to further enhance mobility and environmental adaptability. The use of this skin does not require complex control algorithms or significant modification of the hardware design. The cushioning and backing effects of the inflated skin prevent damage to legged robots by reducing the impact force and minimizing the structural deformation. Based on this newly provided protection, a robot can roll and fall from tall structures with less concern for damage. In addition, through the new type of crawling motion enabled by the volumed form and compliance of the inflated skin, a robot can stably and efficiently pass through structures with a low height while minimizing the loads on the motors. The low-density volume and form of the inflated skin enable sufficient buoyancy and increased drag force on water, respectively. As a result, a legged robot will float stably on water and swim efficiently with simple leg motions. To the best of our knowledge, the quadrupedal robot's ability to perform these locomotion modes is unprecedented, and it was made possible by the comprehensive implementation of the inflatable sensing structure across the robot's entire body.

Furthermore, the tactile sensors integrated with the inflatable skin enable a host robot to overcome obstacles in unstructured environments without visual information. When an unavoidable impact occurs, the robot can immediately detect the impact and take adaptive and protective actions more agilely before losing its stability. Unlike vision sensors, tactile sensors do not require high postprocessing computational costs. Therefore, the inflatable sensing skin efficiently increases the host robot's environmental adaptability from unpredictable external disturbances by improving robot safety, autonomy, and interaction skills.

To increase the usability of the inflatable sensing skin, there is still room for further improvement. One of the most important issues is durability for practical applications in harsh environments. In particular, air leakage from punctures is the most problematic. Unfortunately, it is almost impossible to prevent skin damage altogether. However, self-healable fabrics that instantly recover from damage are actively being developed using nanotechnology.[87–90] In addition, some elastomers contain self-healing capabilities when placed under a particular range of temperatures.[91–94] Therefore, the leakage problem can be addressed by using self-healing fabrics as the skin material or by laminating elastomers onto the thermoplastic sheet layers. Furthermore, recently developed flame-retardant materials can be coated onto the self-healing layer for the implementation of a heat-resistive, durable skin.

Another area for future work is improving the spatial resolution of tactile sensing. The current fabric-based sensors only cover a total of 27 discrete locations. To implement an increased spatial sensing functionality, the detection of continuous contact distribution is necessary. Electrical impedance tomography is a promising sensing method for acquiring continuous contact location data. This sensing technique measures the continuous distribution of the electrical impedance between fabric electrodes, which correlates with the force distribution from external contact.[95–101]

In addition, fabric sensor dead zones, where fabric sensors are not installed, inevitably exist on small and curved areas of the inflated skin surface. This is a critical issue to be addressed for maximizing the skin's sensing coverage. In the sensor performance section, we suggested that contact locations could be approximated by analyzing the output patterns of the air pressure sensors through ANN-based machine learning. Meanwhile, it is worth noting that other types of sensors are often already built into legged robots, such as IMUs, foot pressure sensors, and joint torque sensors, providing different sensing signal patterns depending on the contact locations. Adding such data to the training of a machine learning model is a promising way to improve the localization accuracy and spatial resolution.

In the future, we would also like to implement an accurate method for estimating the directions of the contact forces and use this information for robot control. While external contacts are applied in various directions in a real environment, the proposed inflatable sensing skin measures only the force components in the direction normal to the skin. The most direct approach to measure the direction of force is to integrate three-axis force sensors onto the skin surface. However, few sensors can be robustly attached to a curved and deformable skin surface and would require significant modifications to the design. Therefore, a more realistic approach is fusion of the datasets from the tactile sensors with existing embedded sensors on mobile robots, such as joint torque sensors and foot pressure sensors. Most existing quadruped robots can already detect the presence of external contact from motor current signals.[102,103] Unable to find the exact contact location, these robots assume that the contact is applied around the foot and estimate the force magnitude and direction from its kinematic information. Therefore, if the contact localization from the inflatable sensing skin and the various force direction estimation techniques of built-in sensors are combined, the location, magnitude, and direction of applied forces can be accurately identified. This will allow for more efficient motion planning in response to external forces.

4. Experimental Section

Soft Inflatable Sensing Skin: One of the important considerations when designing an external skin for a legged robot is the weight, since an additional weight caused by the skin may significantly affect the locomotion performance of the host robot. In particular, increasing the mass of the system or changing the center of mass may require upgrading the actuator performance or modifying the control strategy. To avoid this problem, structures for inflatable sensing skin were developed using only lightweight materials, such as plastic sheets and fabrics. The inflatable skin structure was composed of outer and chamber layers made from thermoplastic sheets (Figure 2a). The space between the chamber layers served as an air chamber that can be actively inflated when supplied with compressed air. On the middle layer, fabric-based touch sensors were attached and covered with an outer layer that protects them from external hazards.

**ADVANCED
SCIENCE NEWS**

www.advancedsciencenews.com

**ADVANCED
INTELLIGENT
SYSTEMS**
Open Access

www.advintellsyst.com

The inflatable sensing skin was fabricated using only simple laminating and heat-sealing processes. In addition, the skin was highly conformable to quadruped robots with various shapes through folding and sleeve structures using structural constraints introduced by the heat-sealing process. When the skin was inflated, the inner layer expands inward, compressing the structure of the host robot and allowing it to be adaptively and tightly fixed to the robot. To avoid a situation in which the volume of the inflated skin interrupts the motion of the host robot because of physical interferences between the robot and skin structures, it was necessary to estimate the shape of the fully inflated skin. Shape estimation was possible using modified modeling that obtains the maximum contraction rate of a pouch motor with inextensible zero-thickness layers.[104–106] Note S7 and Figure S26–S28, Supporting Information explain more details about estimating the final shape of the inflated skin depending on structural constraints. Additionally, fabric rubber bands were inserted into both ends of the leg skin close to the joints to reduce the radius and avoid interrupting the motion of the host robot. The fabricated skin withstands a pressure up to 23.11 kPa, providing a sufficient protection effect even for heavy robots (Note S8, Supporting Information).

For the sensing capability of the inflatable skin, the fabric-based touch sensors had a four-layer sandwich structure (Figure 2a). The top and bottom layers were composed of stretchable conductive fabric serving as low impedance electrodes. A piezoresistive fabric layer placed between the two electrodes is integrated with a meshed layer on top of it. The meshed layer provided space between the topmost electrode and the piezoresistive fabric layer to minimize unwanted electrode contact when the sensor is not pressed. The thickness and opening size of the meshed layer determined the sensitivity of the sensor.[107] When mechanical pressure was applied to the sensor's surface, the top conductive fabric was stretched and formed contact with the piezoresistive fabric layer through the openings of the meshed layer. This decreased the electrical resistance across the electrodes as the contact area between the top and the piezoresistive fabric layers increased. Furthermore, a thin plastic plate was placed beneath the sensor to minimize curvature, preventing unwanted sensor output changes when the chamber was inflated. The air pressure sensors were off-the-shelf products. They measured the initial internal air pressure of the chamber inflated by an air pump and detected changes in the pressure using external contacts.

Other Details: The details of the fabrication processes (Note S8 and S9, Supporting Information), the hardware and control systems of the robot (Note S10–S13, Supporting Information), In summary, the inflatable robotic sensing skin was produced through lamination of thermoplastic sheets and fabric-based touch sensors. The custom-designed quadruped robot was prepared by assembling 3D-printed components and integrating the control, the sensor readout, and the air supply systems. To waterproof the robot, we took several steps. First, we covered the hip and knee joints of each leg with plastic sheet sleeves. Next, we sprayed water-resistant material on the surface of the entire robot. Additionally, we covered the cables for power supply and communication with waterproof tape and the same water-resistant material used on the robot's surface. The commercial quadruped robot was used with integration of the inflatable sensing skin, the sensor readout circuits, and the air supply systems.

Supporting Information

Supporting Information is available from the Wiley Online Library or from the author.

Acknowledgements

Conflict of Interest

The authors declare no conflict of interest.

Author Contributions

T.K. designed and implemented inflatable sensing skin and hardware of custom-built quadruped robot systems. S.L. designed and implemented software to control the robot system and data post processing. T.K. and S.L. planned and conducted experiments and application scenarios. T.K. and S.L. also processed and analyzed all data from the experiments and the applications. S.C. and S.H. assisted in fabricating the inflatable sensing skin and carrying out the experiments. Y.-L.P. directed the overall research. T.K., S.L., S.H., and Y.-L.P. wrote and edited the manuscript. All authors responded to revisions in the review process.

Data Availability Statement

The data that support the findings of this study are available in the supplementary material of this article.

Keywords

[1] J. Zhao, J. Gao, F. Zhao, Y. Liu, *Sensors* **2017**, *17*, 2426.
[2] J. Delmerico, S. Mintchev, A. Giusti, B. Gromov, K. Melo, T. Horvat, C. Cadena, M. Hutter, A. Ijspeert, D. Floreano, L. M. Gambardella, R. Siegwart, D. Scaramuzza, *J. Field Rob.* **2019**, *36*, 1171.
[3] X. Gao, J. Li, L. Fan, Q. Zhou, K. Yin, J. Wang, C. Song, L. Huang, Z. Wang, *IEEE Access* **2018**, *6*, 49248.
[4] K. R. Aravind, P. Raja, M. P. Ruiz, *Span. J. Agric. Res.* **2017**, *15*, e02R01.
[5] O. Kermorgant, *Rob. Comput. Integr. Manuf.* **2018**, *53*, 178.
[6] G. Fragapane, D. Ivanov, M. Peron, F. Sgarbossa, J. O. Strandhagen, *Ann. Oper. Res.* **2020**, *308*, 125.
[7] Z. Chong, F. Xie, X. J. Liu, J. Wang, H. Niu, *Rob. Comput. Integr. Manuf.* **2020**, *61*, 101857.
[8] G. Picardi, M. Chellapurath, S. Iacoponi, S. Stefanni, C. Laschi, M. Calisti, *Sci. Rob.* **2020**, *5*, aaz1012.
[9] G. Zhang, S. Ma, Y. Shen, Y. Li, *IEEE Trans. Rob.* **2020**, *36*, 855.
[10] X. Zhou, S. Bi, *Bioinspiration Biomimetics* **2012**, *7*, 041001.
[11] C. D. Bellicoso, M. Bjelonic, L. Wellhausen, K. Holtmann, F. Günther, M. Tranzatto, P. Fankhauser, M. Hutter, *J. Field Rob.* **2018**, *35*, 1311.
[12] S. Kim, P. M. Wensing, *Found. Trends. Rob.* **2017**, *5*, 117.
[13] D. Wisth, M. Camurri, M. Fallon, *IEEE Rob. Autom. Lett.* **2019**, *4*, 4507.
[14] F. Grimminger, A. Meduri, M. Khadiv, J. Viereck, M. Wüthrich, M. Naveau, V. Berenz, S. Heim, F. Widmaier, T. Flayols, J. Fiene, A. Badri-Spröwitz, L. Righetti, *IEEE Rob. Autom. Lett.* **2020**, *5*, 3650.
[15] R. Buchanan, T. Bandyopadhyay, M. Bjelonic, L. Wellhausen, M. Hutter, N. Kottege, *IEEE Rob. Autom. Lett.* **2019**, *4*, 2148.
[16] P. M. Wensing, A. Wang, S. Seok, D. Otten, J. Lang, S. Kim, *IEEE Trans. Rob.* **2017**, *33*, 509.
[17] V. Barasuol, O. A. Villarreal-Magaña, D. Sangiah, M. Frigerio, M. Baker, R. Morgan, G. A. Medrano-Cerda, G. A. Medrano-Cerda, D. Gordon, C. Semini, *Front. Rob. AI* **2018**, *5*, 51.

**ADVANCED
SCIENCE NEWS**

www.advancedsciencenews.com

**ADVANCED
INTELLIGENT
SYSTEMS**
Open Access

www.advintellsyst.com

[18] C. Semini, N. G. Tsagarakis, E. Guglielmino, M. Focchi, F. Cannella, D. G. Caldwell, *Proc. Inst. Mech. Eng. I: J. Syst. Control Eng.* **2011**, *225*, 831.

[19] D. Drotman, S. Jadhav, D. Sharp, C. Chan, M. T. Tolley, *Sci. Robot.* **2021**, *6*, aay2627.

[20] D. Drotman, M. Ishida, S. Jadhav, M. T. Tolley, *IEEE ASME Trans. Mechatron.* **2018**, *24*, 78.

[21] C. Semini, V. Barasuol, J. Goldsmith, M. Frigerio, M. Focchi, Y. Gao, D. G. Caldwell, *IEEE ASME Trans. Mechatron.* **2016**, *22*, 635.

[22] Y. Ding, A. Pandala, C. Li, Y. H. Shin, H. W. Park, *IEEE Trans. Rob.* **2021**, *37*, 1154.

[23] H. W. Park, S. Kim, *Bioinspiration Biomimetics* **2015**, *10*, 025003.

[24] V. S. Medeiros, E. Jelavic, M. Bjelonic, R. Siegwart, M. A. Meggiolaro, M. Hutter, *IEEE Rob. Autom. Lett.* **2020**, *5*, 4172.

[25] P. Fankhauser, M. Hutter, *Res. Features* **2018**, *126*, 54.

[26] M. Hutter, C. Gehring, D. Jud, A. Lauber, C. D. Bellicoso, V. Tsounis, J. Hwangbo, K. Bodie, P. Fankhauser, M. Bloesch, R. Diethelm, S. Bachmann, A. Melzer, M. Hoepflinger, in *Proc. IEEE/RSJ Int. Conf. on Intelligent Robots and Systems (IROS)*, Daejeon, Korea 09–14 October **2016**, pp. 38–44.

[27] M. Hutter, C. Gehring, A. Lauber, F. Gunther, C. D. Bellicoso, V. Tsounis, P. Fankhauser, R. Diethelm, S. Bachmann, M. Bloesch, H. Kolvenbach, M. Bjelonic, L. Isler, K. Meyer, *Adv. Rob.* **2017**, *31*, 918.

[28] J. Carius, R. Ranftl, V. Koltun, M. Hutter, *IEEE Rob. Autom. Lett.* **2019**, *4*, 3013.

[29] F. Jenelten, J. Hwangbo, F. Tresoldi, C. D. Bellicoso, M. Hutter, *IEEE Rob. Autom. Lett.* **2019**, *4*, 4170.

[30] E. Guizzo, *IEEE Spectr.* **2019**, *56*, 34.

[31] H. W. Park, P. M. Wensing, S. Kim, *Int. J. Rob. Res.* **2017**, *36*, 167.

[32] H. W. Park, P. M. Wensing, S. Kim, *Rob. Auton. Syst.* **2021**, *136*, 103703.

[33] G. Bledt, M. J. Powell, B. Katz, J. Di Carlo, P. M. Wensing, S. Kim, in *Proc. IEEE/RSJ Int. Conf. on Intelligent Robots and Systems (IROS)*, Madrid, Spain 01–05 October **2018**, pp. 2245–2252.

[34] J. Di Carlo, P. M. Wensing, B. Katz, G. Bledt, S. Kim, in *Proc. IEEE/RSJ Int. Conf. on Intelligent Robots and Systems (IROS)*, Madrid, Spain 01–05 October **2018**, pp. 7440–7447.

[35] Q. Nguyen, M. J. Powell, B. Katz, J. D. Carlo, S. Kim, in *Proc. IEEE Int. Conf. on Robotics and Automation (ICRA)*, Montreal, QC, Canada 20–24 May **2019**, pp. 7448–7454.

[36] M. Neunert, M. Stäuble, M. Giftthaler, C. D. Bellicoso, J. Carius, C. Gehring, M. Hutter, J. Buchli, *IEEE Rob. Autom. Lett.* **2018**, *3*, 1458.

[37] V. Tsounis, M. Alge, J. Lee, F. Farshidian, M. Hutter, *IEEE Rob. Autom. Lett.* **2020**, *5*, 3699.

[38] J. Lee, J. Hwangbo, L. Wellhausen, V. Koltun, M. Hutter, *Sci. Robot.* **2020**, *5*, abc5986.

[39] J. Carius, F. Farshidian, M. Hutter, *IEEE Rob. Autom. Lett.* **2020**, *5*, 2897.

[40] M. Hutter, C. D. Remy, M. A. Hoepflinger, R. Siegwart, *IEEE/ASME Trans. Mechatron.* **2013**, *18*, 449.

[41] M. Hutter, C. Gehring, M. A. Höpflinger, M. Blösch, R. Siegwart, *IEEE Trans. Rob.* **2014**, *30*, 1427.

[42] M. Bjelonic, R. Grandia, O. Harley, C. Galliard, S. Zimmermann, M. Hutter, in *Proc. IEEE/RSJ Int. Conf. on Intelligent Robots and Systems (IROS)*, Prague, Czech Republic 27 September–01 October **2021**, pp. 8388–8395.

[43] M. G. Catalano, M. J. Pollayil, G. Grioli, G. Valsecchi, H. Kolvenbach, M. Hutter, A. Bicchi, M. Garabini, *IEEE Trans. Rob.* **2022**, *38*, 302.

[44] J.-P. Sleiman, F. Farshidian, M. V. Minniti, M. Hutter, *IEEE Rob. Autom. Lett.* **2021**, *6*, 4688.

[45] Y. Ma, F. Farshidian, T. Miki, J. Lee, M. Hutter, *IEEE Rob. Autom. Lett.* **2022**, *7*, 2377.

[46] J. Hwangbo, J. Lee, A. Dosovitskiy, D. Bellicoso, V. Tsounis, V. Koltun, M. Hutter, *Sci. Rob.* **2019**, *4*, aau5872.

[47] J. Lee, J. Hwangbo, M. Hutter, (Preprint). arXiv:1901.07517, v1, submitted: Jan. **2019**, https://arxiv.org/abs/1901.07517.

[48] R. Baines, S. K. Patiballa, J. Booth, L. Ramirez, T. Sipple, A. Garcia, F. Fish, R. Kramer-Bottiglio, *Nature* **2022**, *610*, 283.

[49] N. S. Usevitch, Z. M. Hammond, M. Schwager, A. M. Okamura, E. W. Hawkes, S. Follmer, *Sci. Rob.* **2020**, *5*, aaz0492.

[50] E. W. Hawkes, L. H. Blumenschein, J. D. Greer, A. M. Okamura, *Sci. Rob.* **2017**, *2*, aan3028.

[51] J. D. Greer, L. H. Blumenschein, R. Alterovitz, E. W. Hawkes, A. M. Okamura, *Int. J. Rob. Res.* **2020**, *39*, 1724.

[52] R. Qi, A. Khajepour, W. W. Melek, T. L. Lam, Y. Xu, *IEEE Trans. Rob.* **2017**, *33*, 594.

[53] P. Ohta, L. Valle, J. King, K. Low, J. Yi, C. G. Atkeson, Y.-L. Park, *Soft Rob.* **2018**, *5*, 204.

[54] T. Kim, S. J. Yoon, Y.-L. Park, *IEEE Rob. Autom. Lett.* **2018**, *3*, 3216.

[55] T. Kim, J. Park, S. J. Yoon, H. W. Park, Y.-L. Park, in *Proc. IEEE Int. Conf. on Soft Robotics (RoboSoft)*, Seoul, Korea 14–18 April **2019**, pp. 257–264.

[56] L. Paya, A. Gil, O. Reinoso, *J. Sens.* **2017**, *3497650*.

[57] D. Kim, D. Carballo, J. D. Carlo, B. Katz, G. Bledt, B. Lim, S. Kim, in *Proc. IEEE Int. Conf. on Robotics and Automation (ICRA)*, Paris, France 31 May–31 August **2020**, pp. 2464–2470.

[58] M. Luneckas, T. Luneckas, D. Udris, D. Plonis, R. Maskeliūnas, R. Damaševičius, *Intel. Serv. Rob.* **2021**, *14*, 9.

[59] J. Mrva, J. Faigl, in *Proc. Int. Workshop on Robot Motion and Control (RoMoCo)*, Poznan, Poland 06–08 July **2015**, pp. 240–245.

[60] J. Fan, S. Wang, Q. Yu, Y. Zhu, *Soft Rob.* **2020**, *7*, 615.

[61] M. Calisti, F. Corucci, A. Arienti, C. Laschi, *Bioinspiration Biomimetics* **2015**, *10*, 046012.

[62] D. Meger, F. Shkurti, D. Cortés Poza, P. Giguère, G. Dudek, in *Proc. IEEE/RSJ Int. Conf. on Intelligent Robots and Systems (IROS)*, Chicago, IL, USA 14–18 September **2014**, pp. 2257–2264.

[63] D. Meger, J. C. G. Higuera, A. Xu, P. Giguere, G. Dudek, in *Proc. IEEE Int. Conf. on Robotics and Automation (ICRA)*, Seattle, WA, USA 26–30 May **2015**, pp. 2332–2338.

[64] H. Kim, J. Lee, *Ocean Eng.* **2017**, *130*, 310.

[65] S. Y. Yoo, H. Shim, B. H. Jun, J. Y. Park, P. M. Lee, *Mar. Technol. Soc. J.* **2016**, *50*, 74.

[66] B. Kwak, J. Bae, *Bioinspiration Biomimetics* **2017**, *12*, 036014.

[67] M. Ishida, D. Drotman, B. Shih, M. Hermes, M. Luhar, M. T. Tolley, *IEEE Rob. Autom. Lett.* **2019**, *4*, 4163.

[68] D. Y. Lee, S. R. Kim, J. S. Kim, J. J. Park, K. J. Cho, *Soft Rob.* **2017**, *4*, 163.

[69] D. Y. Lee, J. S. Koh, J. S. Kim, S. W. Kim, K. J. Cho, *Int. J. Precis. Eng. Manuf.* **2013**, *14*, 1439.

[70] M. Eich, F. Grimminger, F. Kirchner, in *Proc. IEEE Int. Workshop on Safety, Security and Rescue Robotics*, Sendai, Japan 21–24 October **2008**, pp. 35–40.

[71] M. M. Dalvand, M. M. Moghadam, *Auton. Rob.* **2006**, *20*, 3.

[72] Y. S. Kim, G. P. Jung, H. Kim, K. J. Cho, C. N. Chu, *IEEE Trans. Robot.* **2014**, *30*, 1487.

[73] S. S. Yun, J. Y. Lee, G. P. Jung, K. J. Cho, *Int. J. Control Autom. Syst.* **2017**, *15*, 36.

[74] P. Fankhauser, *Perceptive Locomotion for Legged Robots in Rough Terrain*, ETH Zurich **2018**.

[75] P. Fankhauser, M. Bjelonic, C. D. Bellicoso, T. Miki, M. Hutter, in *Proc. IEEE Int. Conf. on Robotics and Automation (ICRA)*, Brisbane, QLD, Australia 21–25 May **2018**, pp. 5761–5768.

[76] G. Xin, W. Wolfslag, H.-C. Lin, C. Tiseo, M. Mistry, *Front. Rob. AI* **2020**, *7*, 48.

[77] C. Semini, V. Barasuol, T. Boaventura, M. Frigerio, M. Focchi, D. G. Caldwell, J. Buchli, *Int. J. Rob. Res.* **2015**, *34*, 1003.

**ADVANCED
SCIENCE NEWS**

www.advancedsciencenews.com

**ADVANCED
INTELLIGENT
SYSTEMS**

www.advintellsyst.com

[78] T. Boaventura, J. Buchli, C. Semini, D. G. Caldwell, *IEEE Trans. Rob.* **2015**, *31*, 1324.

[79] J. Park, J. H. Park, in *Proc. IEEE/RSJ Int. Conf. on Intelligent Robots and Systems (IROS)*, Vilamoura-Algarve, Portugal 07–12 October **2012**, pp. 175–180.

[80] J. Choi, B. Na, S. Oh, K. Kong, in *Proc. IEEE/ASME Int. Conf. on Advanced Intelligent Mechatronics*, Besacon, France 08–11 July **2014**, pp. 72–75.

[81] M. Y. Chuah, S. Kim, *IEEE Sens. J.* **2014**, *14*, 1693.

[82] G. Valsecchi, R. Grandia, M. Hutter, *IEEE Rob. Autom. Lett.* **2020**, *5*, 1548.

[83] X. Zhu, J. Wan, C. Zhou, W. Xu, *Comput. Electr. Eng.* **2021**, *91*, 107027.

[84] J. Hooks, M. S. Ahn, J. Yu, X. Zhang, T. Zhu, H. Chae, D. Hong, *IEEE Rob. Autom. Lett.* **2020**, *5*, 5409.

[85] N. Dini, V. J. Majd, *Mech. Mach. Theory* **2020**, *146*, 103737.

[86] V. Barasuol, J. Buchli, C. Semini, M. Frigerio, E. R. De Pieri, D. G. Caldwell, in *Proc. IEEE Int. Conf. on Robotics and Automation (ICRA)*, Karlsruhe, Germany 06–10 May **2013**, pp. 2554–2561.

[87] Y. Li, B. Ge, X. Men, Z. Zhang, Q. Xue, *Compos. Sci. Technol.* **2016**, *125*, 55.

[88] H. Zhou, H. Wang, H. Niu, T. Lin, *Adv. Mater. Interfaces* **2018**, *5*, 1800461.

[89] M. Wu, B. Ma, T. Pan, S. Chen, J. Sun, *Adv. Funct. Mater.* **2016**, *26*, 569.

[90] C.-H. Xue, X. Bai, S. T. Jia, *Sci. Rep.* **2016**, *6*, 27262.

[91] M. D. Hager, P. Greil, C. Leyens, U. S. Schubert, *Adv. Mater.* **2010**, *22*, 5424.

[92] S. Terryn, J. Brancart, D. Lefeber, G. V. Assche, B. Vanderborght, *Sci. Rob.* **2017**, *2*, aan4268.

[93] R. A. Bilodeau, R. K. Kramer, *Front. Rob. AI* **2017**, *4*, 48.

[94] Y. Cao, Y. J. Tan, S. Li, W. W. Lee, H. Guo, Y. Cai, C. Wang, B. C.-K. Tee, *Nat. Electron.* **2019**, *2*, 75.

[95] H. Lee, K. Park, J. Kim, K. J. Kuchenbecker, in *Proc. IEEE Int. Conf. on Robotics and Automation (ICRA)*, Montreal, QC, Canada 20–24 May **2019**, pp. 5411–5417.

[96] H. Lee, D. Kwon, H. Cho, I. Park, J. Kim, *Sci. Rep.* **2017**, *7*, 39837.

[97] H. Lee, K. Park, J. Kim, K. J. Kuchenbecker, in *Int. AsiaHaptics conference*, Springer, Singapore **2018**, pp. 107–109.

[98] K. Park, H. Park, H. Lee, S. Park, J. Kim, in *Proc. IEEE Int. Conf. on Robotics and Automation (ICRA)*, Paris, France 31 May **2020**, pp. 1617–1624.

[99] K. Liu, Y. Wu, S. Wang, H. Wang, H. Chen, B. Chen, J. Yao, *Adv. Intell. Syst.* **2020**, *2*, 1900161.

[100] X. Duan, S. Taurand, M. Soleimani, *Sci. Rep.* **2019**, *9*, 8831.

[101] F. Visentin, P. Fiorini, K. Suzuki, *Sensors* **2016**, *16*, 1928.

[102] Z. Cong, A. Honglei, C. Wu, L. Lang, Q. Wei, M. Hongxu, *IEEE Access* **2020**, *8*, 161175.

[103] V. Barasuol, G. Fink, M. Focchi, D. Caldwell, C. Semini, in *Proc. Int. Conf. on Climbing and Walking Robots and the Support Technologies for Mobile Machines (CLAWAR)*, Kuala Lumpur, Malaysia 26–28 August **2019**, pp. 99–106.

[104] R. Niiyama, D. Rus, S. Kim, *Proc. IEEE Int. Conf. on Robotics and Automation (ICRA)*, Hong Kong, China 31 May–5 Jun **2014**, 6332.

[105] J. Kwon, S. J. Yoon, Y.-L. Park, *IEEE Trans. Rob.* **2020**, *36*, 743.

[106] C.-P. Chou, B. Hannaford, *IEEE Trans. Rob. Autom.* **1996**, *12*, 90.

[107] M. Bianchi, R. Haschke, G. Büscher, S. Ciotti, N. Carbonaro, A. Tognetti, *Electronics* **2016**, *5*, 42.